

Correlated states controlled by tunable van Hove singularity in moiré WSe₂

Patrick Knüppel^{1*}, Jiacheng Zhu^{2*}, Yiyu Xia², Zhengchao Xia², Zhongdong Han¹, Yihang Zeng¹, Kenji Watanabe³, Takashi Taniguchi³, Jie Shan^{1,2,4**}, Kin Fai Mak^{1,2,4**}

¹Laboratory of Atomic and Solid-State Physics, Cornell University, Ithaca, NY, USA

²School of Applied and Engineering Physics, Cornell University, Ithaca, NY, USA

³National Institute for Materials Science, 1-1 Namiki, 305-0044 Tsukuba, Japan

⁴Kavli Institute at Cornell for Nanoscale Science, Ithaca, NY, USA

*These authors contributed equally

**Email: jie.shan@cornell.edu; kinfai.mak@cornell.edu

Twisted bilayers of transition metal dichalcogenide (TMD) semiconductors have emerged as a highly tunable system for the studies of correlated and topological states of matter, such as superconductivity¹, ferromagnetism², correlated insulators³⁻⁵, and topological and Chern insulators⁶⁻¹². However, the connection between these symmetry-breaking ground states and the underlying band structure singularity in these materials¹³⁻¹⁶ remains largely unexplored. Here, by combining exciton sensing and magnetic circular dichroism (MCD) measurements, we demonstrate how the magnetic properties and the correlated insulating states are controlled by the gate-tunable van Hove singularity (VHS) in the band structure of twisted bilayer WSe₂ (tWSe₂). In particular, we demonstrate how the location of the VHS in the tWSe₂ band structure can influence 1) the stability of Stoner ferromagnetism, 2) the valley polarizability and the stability of Chern insulators, as well as 3) the layer polarizability and the associated metal-insulator transition. The results are supported by continuum model^{17,18} band structure calculations. Our work highlights an important ingredient for understanding the electronic phase diagram in twisted bilayer TMDs.

Main

The diverging density of states (DOS) at a VHS in the electronic band structure of materials is expected to strongly enhance the effects of electron-electron interactions and give rise to a multitude of correlated states of matter, such as the Stoner ferromagnetism¹⁹, superconductivity²⁰ and correlated insulators. The limited ability to control the DOS at the Fermi energy in bulk materials has, however, hindered a controllable and systematic study on the connection between the symmetry-breaking ground states and the location of the VHS relative to the Fermi level. The emergence of moiré materials²¹⁻²⁵, which support highly tunable electronic band structure and Fermi level, provides an opportunity to address this question and help understand the emergence of strongly correlated matter.

The family of semiconducting moiré materials built on TMDs is an appealing platform due to its tunable electronic correlations and topology²¹. In particular, twisted bilayer TMDs (tTMDs), which host a honeycomb/triangular moiré lattice (depending on the twist angle²⁶), are known to have spin/valley-polarized flat Chern bands^{17,18,27-32}. A suite of exotic states and phenomena, such as integer⁷ and fractional Chern insulators^{6,8,11,12}, fractional

topological insulators⁹, superconductivity¹, ferromagnetism² and metal-insulator transitions^{3,5,33}, has been demonstrated by recent experiments. Band structure calculations have shown that both the bandwidth and band topology of the flat bands are tunable by an electric field perpendicular to the sample plane, which continuously tunes the interlayer potential difference^{13,17,18}. The electric field can also tune the location of the VHS in band fillings^{3,5,13,15,16,33}, which has been suggested to closely connect to the stability of the correlated insulating states at integer moiré lattice fillings^{13–16,27}. However, a systematic experimental study on the relationship between the VHS and the symmetry-breaking ground states is missing to date.

In this study, we combine exciton sensing³⁴ and magnetic circular dichroism (MCD) measurements³⁵ to investigate the strong impact of the VHS on the electronic and magnetic properties of tWSe₂. Figure 1a shows the dual-gated device structure employed in this study. The top and bottom gate voltage can independently control the moiré lattice filling factor (ν) of and the perpendicular electric field (E) through the tWSe₂ sample. We also employ a WS₂ monolayer as an exciton sensor, which is spatially separated from the sample by a thin hexagonal boron nitride (hBN) spacer (about 1 nm thick). Because of the type-II band alignment in WSe₂/WS₂ heterostructures³⁶, the WS₂ sensor is charge neutral in our experiment. The energy of the 2s exciton Rydberg state in the sensor is sensitive to the compressibility of the sample due to dielectric screening of the sensor exciton binding energy³⁷; in particular, a blue-shift and an enhanced spectral weight in the 2s resonance correspond to the emergence of an incompressible state in the sample³⁴. See Methods for details on device fabrication, optical reflection contrast and MCD measurements, and band structure calculations.

We focus on a 2.7-degree tWSe₂ sample in this study (see Extended Data Fig. 1 and 2 for main results on other twist angles and Methods for twist angle or moiré density calibration). Figure 1b shows the continuum model band structure under $E = 0$ in the moiré Brillouin zone and the corresponding energy-dependent DOS. We have reproduced the reported band structure^{17,18}. In particular, the two topmost moiré valence bands are spin/valley-resolved Chern bands with Chern number +1 at the K-valley (opposite sign of Chern number at the K'-valley); the VHS aligns with the saddle-point singularity at the m -point of the moiré Brillouin zone.

Figure 1c shows the spectrally averaged reflection contrast of the fundamental moiré exciton resonance of tWSe₂ as a function of ν and E (see Extended Data Fig. 3 for reflection contrast spectra). Unless otherwise specified in the following, all results are presented at a measurement temperature of $T = 1.6$ K. We observe an enhanced reflection contrast for $0 < \nu < 1$ in the layer-hybridized region of the electrostatics phase diagram (bound by the dashed lines, see Methods and Extended Data Fig. 4). The layer-hybridized region is centered at $E = 0$ (as expected for twisted homobilayers). The critical electric field separating the layer-hybridized and -polarized regions increases with ν because electrostatics requires a larger electric field to fully polarize a higher density of charge carriers to the top/bottom WSe₂ layer. The moiré bands are Chern bands in the layer-hybridized region (Fig. 1b); they become topologically trivial and more dispersive in the

layer-polarized region (Extended Data Fig. 5). The results are fully consistent with the reported studies on tMoTe₂ (Ref. ^{6,8,17,18}).

Figure 1d shows the corresponding dependence for the integrated reflection contrast of the 2s resonance of the sensor for comparison (see Extended Data Fig. 3 for the reflection contrast spectra near the 2s resonance). Correlated insulating states, which correspond to an enhanced 2s reflection contrast, are observed near $\nu = 1, 1/3, 1/4$ and $1/6$ only in the layer-hybridized region. These states turn compressible in the layer-polarized region. (An asymmetry for $E > 0$ and $E < 0$ is also observed because the sensor is closer to the top WSe₂ layer.) The results are consistent with the more dispersive moiré bands (thus with weaker correlation effects) in the layer-polarized region.

Stoner ferromagnetism

We examine the magnetic properties of the tWSe₂ sample by MCD measurements near the fundamental moiré exciton resonance (see Extended Data Fig. 3 for MCD spectra). Figure 2a shows the spontaneous MCD signal integrated over the moiré exciton resonance (Methods) as a function of ν and E . A spontaneous MCD hot spot is observed near $\nu = 0.8$ and $E = 0$. The MCD at the hot spot shows a clear magnetic hysteresis with a coercive field around 10 mT (Fig. 2b). The spontaneous MCD and the hysteresis disappears at a transition temperature about 3 K. The results clearly demonstrate the emergence of ferromagnetism in a compressible region of the electrostatics phase diagram (i.e. metallic ferromagnetism).

To gain insight on the metallic ferromagnetism, we study the MCD under a small out-of-plane magnetic field ($B = 0.5$ T) as a function of ν and E (Fig. 2c). (See Extended Data Fig. 6 for similar MCD maps at higher magnetic fields.) The signal is proportional to the magnetic susceptibility of the sample except at the ferromagnetic region of the phase diagram, where the system is spontaneously ordered. The MCD (or susceptibility) is enhanced in the layer-hybridized region for $0 < \nu < 1$; the signal is also sensitive to the incompressible states at fractional fillings. An enhanced MCD region is also observed for $\nu > 1$; the region shows a dispersion in the $\nu - E$ plane and displays a wing-like structure. We mark the region with enhanced MCD by dashed lines.

We perform band structure calculations under varying electric fields (or interlayer potential difference) in order to understand the observations in Fig. 2 (Methods). Figure 2d shows the electronic DOS as a function of ν and E in the experimentally relevant region of the phase diagram. In general, higher DOS is seen in the layer-hybridized region at $\nu < 1$, where the moiré bands are more flat (Extended Data Fig. 5). A VHS with diverging DOS is observed near $\nu = 0.7$ at $E = 0$; the VHS disperses towards higher fillings with increasing electric field and displays a wing-like structure. The DOS map in Fig. 2d is well correlated with the MCD/susceptibility map in Fig. 2c except at the commensurate fillings $\nu = 1, 1/3$ and $1/4$, where the strong electronic correlations and the emergence of local magnetic moments in these correlated insulating states lead to a complete breakdown of the band picture. The overall agreement between experiment and theory is expected because the magnetic susceptibility of a Landau Fermi liquid is proportional to the electronic DOS³⁸; in particular, the susceptibility is substantially enhanced at the VHS.

At $B = 0$, the highest DOS at the VHS near $\nu = 0.7$ and $E = 0$ gives rise to the observed metallic ferromagnetism (the spontaneous MCD hot spot) in Fig. 2a; the ferromagnetic state disappears with increasing E as the DOS at the VHS decreases (Extended Data Fig. 5). The result supports a Stoner mechanism for the observed metallic ferromagnetism. In particular, only the highest DOS at the VHS near $E = 0$ is able to fulfill the Stoner criterion¹⁹ and stabilize spontaneous magnetic ordering. Note that the small discrepancy for the location of the spontaneous MCD hot spot and the calculated VHS is likely caused by the choice of continuum model parameters and/or interaction effects not accounted for in the single-particle continuum model.

To further support the assignment of the enhanced magnetic susceptibility and ferromagnetism to a VHS-origin, we correlate the MCD results with electrical transport measurements in another device with 3.5-degree tWSe₂ (Extended Data Fig. 7). The VHS in the electronic structure is manifested in the transport measurements as a local resistivity maximum. The location of these transport features in the electrostatics phase diagram closely matches with that for the enhanced MCD, confirming our picture of VHS-enhanced magnetic response. Note that no metallic ferromagnetism is observed in the 3.5-degree sample; this is reasonable given the weaker correlation effects in larger twist angle samples.

Valley polarizability and Chern insulating state

Next we examine how the VHS affects the magnetic properties and the nature of the $\nu = 1$ correlated insulating state under high magnetic fields. Figure 3a shows the MCD as a function of ν and B at $E = 0$. A selected line cut at $\nu = 1$ together with the field derivative of MCD ($\frac{dMCD}{dB}$) are shown in Fig. 3b (see Extended Data Fig. 8 for line cuts at other fillings). The MCD increases with B and displays a bump near $B = 1.5$ T, beyond which it saturates (i.e. fully spin/valley-polarized). Correspondingly, the differential magnetic susceptibility, as represented by $\frac{dMCD}{dB}$, shows a peak near $B = 1.5$ T. The result suggests a metamagnetic transition to a spin/valley-polarized state near the saturation field $B_s \approx 1.5$ T. We summarize in Fig. 3a the filling factor dependence of B_s (determined at 85% of the saturated MCD value) and the zero-field magnetic susceptibility $\left. \frac{dMCD}{dB} \right|_{B=0}$. The latter diverges near $\nu = 0.8$, where ferromagnetism develops; B_s increases from zero near $\nu = 0.8$, shows a bump at $\nu = 1$ and increases quickly for $\nu > 1$.

We further investigate the evolution of the correlated insulating states with B in Fig. 3c, which shows the 2s reflection contrast of the sensor as a function of ν and B at $E = 0$. In the same plot, we also show the filling factor dependence of B_s for comparison. In addition to the fractional states that do not show obvious dependence on B , two correlated insulating states emerge for $B \gtrsim B_s$ near $\nu = 1$: one with filling factor independent of B and the other with filling factor dispersing with B .

The insulating states that do not disperse with B are non-topological correlated insulators; in particular, the fractional states are likely generalized Wigner crystals^{34,39}. On the other hand, the state dispersive with B is a Chern insulator. Using the quantum oscillations in the

sample to calibrate the gate capacitances (Methods and Extended Data Fig. 9), we can obtain the twist angle of the tWSe₂ sample and a Chern number $c = 1$ for the Chern insulator. The Chern insulator emerges only after full spin/valley polarization is achieved beyond the metamagnetic transition near B_s ; this is expected for the spin/valley-resolved Chern bands in tWSe₂ (Fig. 1b). The existence of both the non-topological and Chern insulators for $B > B_s$ near $\nu = 1$ suggests that the two states are competing and close in the ground state energy. This is in contrast to tMoTe₂, in which only the Chern insulator is observed near $\nu = 1$ irrespective of B (Ref. ^{6,8}). Prior to full spin/valley polarization (i.e. $B < B_s$), only the non-topological insulator remains. The insulator is a possible valley-coherent state¹³ that can undergo a metamagnetic transition near B_s to a spin/valley-polarized state.

Interestingly, a closer inspection on Fig. 3c reveals a bump in the 2s reflection contrast of the sensor that closely traces the saturation field B_s . The result suggests a close connection between magnetic saturation (or full spin/valley-polarization) and the underlying electronic structure of the material. To understand this observation, we calculate the electronic DOS as a function of ν and B (at $E = 0$) in Fig. 3d. (Note that for simplicity we only take into account the Zeeman effect in our calculations.) The VHS with large DOS splits under B with one dispersing to a higher filling factor and crossing $\nu = 1$ near $B \approx 4$ T. The good match between the location of the VHS in Fig. 3d and the 2s bump in Fig. 3c supports the 2s bump traces the underlying VHS in the band structure; in particular, the presence of a VHS in the sample layer is expected to modify the dielectric screening of the exciton binding in the sensor layer, leading to the observed 2s bump. The results demonstrate a close connection between the VHS in the band structure and the transition/crossover to a fully spin/valley-polarized state near B_s and the subsequent emergence of the Chern insulator near $\nu = 1$. Note that 2s sensing is not able to capture the VHS dispersing to lower filling factors, where correlated states at fractional fillings emerge; this is likely caused by the breakdown of the single-particle band picture in this strongly correlated regime of the phase diagram.

Metal-insulator transition at $\nu = 1$

Finally, we examine the connection of the VHS to the electric-field-tuned metal-insulator transition (MIT) at $\nu = 1$ in tWSe₂. Figure 4a shows the sensor 2s reflection contrast as a function of ν and E ($B = 0$). A transition at $\nu = 1$ from a correlated insulating state to a compressible metallic state near a critical electric field $E_c = 60$ mV/nm is observed. The result is consistent with the reported electric-field-tuned MIT⁵. We further characterize the MIT by the electric field dependence of the magnetic susceptibility ($\propto \left. \frac{dMCD}{dB} \right|_{B=0}$) at $\nu = 1$ and varying temperatures (Fig. 4b). A strong temperature dependence following the Curie-Weiss behavior (Extended Data Fig. 10) is observed in the insulating phase for $E < E_c$; in contrast, the metallic phase for $E > E_c$ shows a much weaker temperature dependence. The results demonstrate the emergence of local magnetic moments due to Coulomb-localization of the charge carriers in the insulating phase⁴⁰; the behavior transitions to that of a metallic Pauli susceptibility for $E > E_c$ ⁴¹.

In Fig. 4a, we also trace the location of the VHS (as determined by the enhanced susceptibility in Fig. 2c) and the phase boundary separating the layer-hybridized and -polarized regions (Fig. 1c,d). The 2s reflection contrast is slightly enhanced when the VHS crosses the $\nu = 1$ insulating state, suggesting a VHS-enhanced charge gap for the insulator. Interestingly, the MIT critical point E_c is in close proximity to both the VHS location and the layer-polarization phase boundary at $\nu = 1$. This observation suggests a close connection between the electronic VHS, the layer polarizability and the electric-field-tuned MIT in tWSe₂. In fact, a recent theory study has pointed out the importance of the VHS in driving the MIT in the material and in determining the magnetic properties near the MIT¹⁶. Our results are largely consistent with this theory and provide further guidance in understanding the physics of the MIT at $\nu = 1$ in future studies.

Conclusions

In summary, by combining observables for the electronic compressibility and magnetization together with continuum model calculations, we develop a cohesive understanding of the electronic phase diagram in tWSe₂ and its connection to the VHS in the band structure. Our work also bridges the gap^{26,42} between the previously explored small⁷ and large^{3,5,33} twist angle limits and will allow further engineering of the correlated states in this material. Interesting future directions include the search for superconductivity enhanced by the VHS as well as exciton condensation involving strongly correlated Chern bands⁴³.

Methods

Device fabrication

Twisted WSe₂ moiré devices were assembled using the layer-by-layer dry transfer method⁴⁴. Details have been reported in earlier studies^{4,6}. In short, thin flakes of hexagonal boron nitride (hBN), few layer thick graphite, monolayer WSe₂ and monolayer WS₂ were exfoliated and isolated on Si/SiO₂ wafers. Optical reflection color contrast was used to identify appropriate flake shapes and thicknesses. A thin film of polycarbonate on polydimethylsiloxane (PDMS) was employed as a stamp to pick up the layers in sequence from top to bottom (Fig. 1a), after which the device was released onto a Si/SiO₂ substrate with prepatterned Platinum gate electrodes at 180°C. To create the moiré pattern, a single flake of WSe₂ monolayer was mechanically cut in half using an AFM tip, and the two parts were picked up with a target twist angle θ .

Optical reflection contrast and MCD measurements

Optical measurements were performed in a closed-cycle cryostat (Attocube, Attodry 2100) with magnetic fields up to 9 T along the optical axis, perpendicular to the twisted WSe₂ device held at temperatures down to $T = 1.6$ K. A halogen lamp (for 2s sensing and MCD) or LED (only for MCD) was used interchangeably as broadband CW light sources. The input light was spatially filtered by a single mode fiber and sent into the cryostat as collimated beam. A low temperature microscope objective (Attocube, NA = 0.8) was used to focus the light tightly onto the sample. The intensity was kept below 50 nW/ μm^2 , to avoid affecting the sample magnetization. We found that reducing the incident power by an order of magnitude does not lead to changes in the observed quantities. The reflected

light was collected and delivered to a spectrometer and liquid nitrogen cooled CCD array to measure the reflection spectrum R . To obtain the reflection contrast spectrum (RC), we acquired a reference spectrum R_0 at a high doping density, where the excitonic resonances are mostly quenched, and normalized the differential reflection spectrum $R - R_0$ to R_0 as $(R - R_0)/R_0$.

Reflective magnetic circular dichroism (MCD) was used to study the magnetization and magnetic susceptibility of the sample. A linear polarizer and quarter wave plate were used to generate circularly polarized incident light σ^- and σ^+ , which allow the separate collection of the reflection spectra R^- and R^+ . The MCD spectrum was calculated as $\text{MCD} = (R^- - R^+)/ (R^- + R^+)$. As the reflection spectrum depends on tuning parameters such as doping, displacement field and magnetic field, a broad range of wavelengths (725 to 745 nm or 1.66 to 1.71 eV) around the 1s exciton resonances of tWSe₂ was chosen to average the absolute value of MCD (“spectrally averaged MCD”, as displayed in Fig. 2a). The resonances of tWSe₂ and the MCD analysis procedure are illustrated in Extended Data Fig. 3a and 3b, respectively. The same spectral integration range was used to obtain the spectrally averaged reflectance after summing the two circular polarizations, as displayed in Fig. 1c. Magnetic susceptibility was estimated by linearly fitting the MCD response at small magnetic fields $|B| \leq 0.5$ T. Magnetic saturation field B_s was defined at the field where the MCD signal (or sample magnetization) reaches 85% of its saturated value. To estimate the differential susceptibility (shown in Fig. 3b), a Savitzky–Golay filter was applied to obtain a smoothed numerical derivative from the data to reduce the impact of measurement noise.

Determination of phase boundaries

The phase space boundary for layer hybridization was estimated using the electric field dependence of the moiré exciton reflection contrast (Extended Data Fig. 4). The boundary is defined at the extrema of the electric field derivative of integrated reflection contrast. A similar method has been employed previously in Ref. ². In particular, the critical electric field at $\nu = 1$ following this method is $E_c = 60$ meV/nm. We repeat the procedure for fillings in $0.8 \leq \nu \leq 1$, where the RC derivative displays a clear peak at the critical electric field, and fit a smooth cubic spline to obtain a boundary curve. To generate a guide the eye, as shown in Figs. 1c and 1d, we extrapolate the curve to $(\nu, E) = (0, 0)$. To define the phase space with enhanced magnetic susceptibility in Fig. 2c, we use a threshold value of 3% for the integrated MCD value at $B = 0.5$ T and delineate its boundary.

Optical sensing of compressibility

Variations in the sample compressibility modulate the dielectric environment of the sensor layer³⁷, which can be read out by optical spectroscopy of the sensor layer^{34,45–47}. Monolayer WS₂ was chosen for optical sensing of the electronic compressibility in tWSe₂. The relative band alignments of the valence bands allow for the sensor layer to remain charge neutral over the entire range of hole densities and displacement fields used throughout this study. Reflection contrast of the sensing layer was normalized by a background spectrum acquired upon electron doping the sensor layer. Such a normalized spectrum is displayed in Extended Data Fig. 3c, as a function of hole doping in the sample. Accidentally, there are higher lying excitonic states in the same frequency range as the 2s Rydberg WS₂ exciton

which we utilize for sensing purposes. We therefore removed a broad third order polynomial background across the wavelength range shown in Extended Data Fig 3c to arrive at the spectra shown in 3d. This allows us to trace the energy of the 2s exciton peak (black dots) and integrate a 2 nm wavelength window around the peak to extract the integrated RC contrast (as shown for example in Fig. 1d). This yields a more accurate measure of the sample incompressibility compared to integration of a fixed wavelength window due to the large variations in exciton energy as the filling factor of tWSe₂ is varied.

Twist angle calibration

In order to calibrate the twist angle θ and the moiré density n_M for the sample examined in the main text, we measured the MCD spectrum at a large magnetic field (8.8 T) and counted the number of filled Landau levels (LLs) as the gate voltage increases (Extended Data Fig. 9a). An interval of about 1.5V corresponds to 5 filled LLs, from which we deduce a carrier density increase of $7 \times 10^{11} \text{ cm}^{-2}$ per Volt between filling 0 and 1, as shown in Extended Data Fig. 9b. We then used the sensor layer to independently measure the gate voltages at the correlated insulating states (Extended Data Fig. 9c), from which $n_M \approx (2.4 \pm 0.1) \times 10^{12} \text{ cm}^{-2}$ and $\theta \approx (2.7 \pm 0.1)$ degrees can be obtained. We notice a slight increase in the LL period for $\nu \leq 1$, which we accounted for by using a two-piece linear interpolation of the experimental data points above and below the insulating states at filling factor 1 (including the Chern insulating states). The above results further allow us to determine the hBN thickness for the top and bottom gates: $d_{\text{tg}} = 18 \text{ nm}$ and $d_{\text{bg}} = 15 \text{ nm}$, respectively. The experimental electric field can then be obtained as $E = V_{\text{tg}}/2d_{\text{tg}} - V_{\text{bg}}/2d_{\text{bg}} - E_0$ (V_{tg} and V_{bg} denote the top and bottom gate voltage, respectively). We attribute a constant offset $E_0 = 13 \text{ mV/nm}$ to a built-in field from the asymmetry of the device due to the presence of the sensing layer.

Band structure calculations

The single-particle band structure and density of state calculations are based on the continuum model for twisted TMD homobilayer following Ref. ^{17,18}. For the K-valley, the two-band Hamiltonian with momentum \mathbf{k} and effective mass m^* reads

$$H_K = \begin{pmatrix} \frac{-\hbar\mathbf{k}^2}{2m^*} + \Delta_b(\mathbf{r}) + \frac{V_z}{2} & \Delta_T(\mathbf{r}) \\ \Delta_T^\dagger(\mathbf{r}) & \frac{-\hbar\mathbf{k}^2}{2m^*} + \Delta_t(\mathbf{r}) - \frac{V_z}{2} \end{pmatrix},$$

where $\Delta_{b,t}(\mathbf{r})$ and $\Delta_T(\mathbf{r})$ are the bottom and top layer energies and the interlayer tunneling amplitude, respectively. An additional interlayer potential difference is introduced with V_z , which can be tuned experimentally with an out-of-plane electric field. To model the moiré lattice structure, the terms are approximated as $\Delta_{b,t}(\mathbf{r}) = 2V \sum_{j=1,3,5} \cos(\mathbf{G}_j \mathbf{r} \pm \psi)$ and $\Delta_T(\mathbf{r}) = w(1 + e^{i\mathbf{G}_2 \mathbf{r}} + e^{i\mathbf{G}_3 \mathbf{r}})$ with reciprocal lattice vectors \mathbf{G}_j and parameters V, ψ, w for the moiré lattice depth, shape and interlayer tunneling strength. The specific model parameters for tWSe₂ were taken from Ref. ¹⁸ to be $(V, \psi, w) = (9 \text{ meV}, 128^\circ, 18 \text{ meV})$. The lattice constant of WSe₂ for this model is taken as $a = 3.317 \text{ \AA}$ and the effective hole mass as $m^* = 0.43 m_0$ (m_0 is the free electron mass). The Hamiltonian was cut off at the 5th

shell in momentum space. The computed density of states is smoothened using a Gaussian filter with a full width at half maximum of 1 meV. To facilitate comparison to experiments, the interlayer potential difference was converted to electric field using a dipole moment of $0.26 \text{ e} \cdot \text{nm}^{41}$. To include the effect of an out-of-plane magnetic field, a Zeeman energy shift was added between the time-reversed copies of K- and K'-valleys, using a hole g -factor of 10. Specifically, the band structure was first calculated without accounting for the magnetic field. Two copies for the K- and K'-valley band structures were then displaced in energy by 0.58 meV per Tesla and added to obtain an approximation to the band structure at finite magnetic field.

Acknowledgements

We thank Kaifei Kang, Ligu Ma and Liang Fu for fruitful discussions.

References

1. Xia, Y. *et al.* Unconventional superconductivity in twisted bilayer WSe₂. Preprint at <https://doi.org/10.48550/arXiv.2405.14784> (2024).
2. Anderson, E. *et al.* Programming correlated magnetic states with gate-controlled moiré geometry. *Science* **381**, 325–330 (2023).
3. Wang, L. *et al.* Correlated electronic phases in twisted bilayer transition metal dichalcogenides. *Nat. Mater.* **19**, 861–866 (2020).
4. Xu, Y. *et al.* A tunable bilayer Hubbard model in twisted WSe₂. *Nat. Nanotechnol.* **17**, 934–939 (2022).
5. Ghiotto, A. *et al.* Quantum criticality in twisted transition metal dichalcogenides. *Nature* **597**, 345–349 (2021).
6. Zeng, Y. *et al.* Thermodynamic evidence of fractional Chern insulator in moiré MoTe₂. *Nature* **622**, 69–73 (2023).
7. Foutty, B. A. *et al.* Mapping twist-tuned multiband topology in bilayer WSe₂. *Science* **384**, 343–347 (2024).

8. Cai, J. *et al.* Signatures of fractional quantum anomalous Hall states in twisted MoTe₂.
Nature **622**, 63–68 (2023).
9. Kang, K. *et al.* Evidence of the fractional quantum spin Hall effect in moiré MoTe₂.
Nature **628**, 522–526 (2024).
10. Kang, K. *et al.* Observation of the double quantum spin Hall phase in moiré WSe₂. Preprint at <https://doi.org/10.48550/arXiv.2402.04196> (2024).
11. Park, H. *et al.* Observation of fractionally quantized anomalous Hall effect.
Nature **622**, 74–79 (2023).
12. Xu, F. *et al.* Observation of Integer and Fractional Quantum Anomalous Hall Effects in Twisted Bilayer MoTe₂. *Phys. Rev. X* **13**, 031037 (2023).
13. Bi, Z. & Fu, L. Excitonic density wave and spin-valley superfluid in bilayer transition metal dichalcogenide. *Nat Commun* **12**, 642 (2021).
14. Hsu, Y.-T., Wu, F. & Das Sarma, S. Spin-valley locked instabilities in moiré transition metal dichalcogenides with conventional and higher-order Van Hove singularities. *Phys. Rev. B* **104**, 195134 (2021).
15. Zang, J., Wang, J., Cano, J. & Millis, A. J. Hartree-Fock study of the moiré Hubbard model for twisted bilayer transition metal dichalcogenides. *Phys. Rev. B* **104**, 075150 (2021).
16. Zang, J., Wang, J., Cano, J., Georges, A. & Millis, A. J. Dynamical Mean-Field Theory of Moiré Bilayer Transition Metal Dichalcogenides: Phase Diagram, Resistivity, and Quantum Criticality. *Phys. Rev. X* **12**, 021064 (2022).

17. Wu, F., Lovorn, T., Tutuc, E., Martin, I. & MacDonald, A. H. Topological Insulators in Twisted Transition Metal Dichalcogenide Homobilayers. *Phys. Rev. Lett.* **122**, 086402 (2019).
18. Devakul, T., Crépel, V., Zhang, Y. & Fu, L. Magic in twisted transition metal dichalcogenide bilayers. *Nat Commun* **12**, 6730 (2021).
19. Stoner, E. C. Collective electron ferromagnetism. *Proceedings of the Royal Society of London. Series A. Mathematical and Physical Sciences* **165**, 372–414 (1997).
20. Bardeen, J., Cooper, L. N. & Schrieffer, J. R. Theory of Superconductivity. *Phys. Rev.* **108**, 1175–1204 (1957).
21. Mak, K. F. & Shan, J. Semiconductor moiré materials. *Nat. Nanotechnol.* **17**, 686–695 (2022).
22. Kennes, D. M. *et al.* Moiré heterostructures as a condensed-matter quantum simulator. *Nat. Phys.* **17**, 155–163 (2021).
23. Balents, L., Dean, C. R., Efetov, D. K. & Young, A. F. Superconductivity and strong correlations in moiré flat bands. *Nat. Phys.* **16**, 725–733 (2020).
24. Andrei, E. Y. & MacDonald, A. H. Graphene bilayers with a twist. *Nat. Mater.* **19**, 1265–1275 (2020).
25. Andrei, E. Y. *et al.* The marvels of moiré materials. *Nat Rev Mater* **6**, 201–206 (2021).
26. Crépel, V. & Millis, A. Bridging the small and large in twisted transition metal dichalcogenide homobilayers: a tight binding model capturing orbital interference and

topology across a wide range of twist angles. Preprint at

<http://arxiv.org/abs/2403.15546> (2024).

27. Pan, H., Wu, F. & Das Sarma, S. Band topology, Hubbard model, Heisenberg model, and Dzyaloshinskii-Moriya interaction in twisted bilayer WSe₂. *Phys. Rev. Res.* **2**, 033087 (2020).
28. Li, H., Kumar, U., Sun, K. & Lin, S.-Z. Spontaneous fractional Chern insulators in transition metal dichalcogenide moiré superlattices. *Phys. Rev. Res.* **3**, L032070 (2021).
29. Yu, H., Chen, M. & Yao, W. Giant magnetic field from moiré induced Berry phase in homobilayer semiconductors. *National Science Review* **7**, 12–20 (2020).
30. Zhang, X.-W. *et al.* Polarization-driven band topology evolution in twisted MoTe₂ and WSe₂. *Nat Commun* **15**, 4223 (2024).
31. Jia, Y. *et al.* Moiré fractional Chern insulators. I. First-principles calculations and continuum models of twisted bilayer MoTe_2 . *Phys. Rev. B* **109**, 205121 (2024).
32. Xu, C., Mao, N., Zeng, T. & Zhang, Y. Multiple Chern bands in twisted MoTe₂ and possible non-Abelian states. Preprint at <https://doi.org/10.48550/arXiv.2403.17003> (2024).
33. Wei, L. *et al.* Linear resistivity at van Hove singularities in twisted bilayer WSe₂. *Proceedings of the National Academy of Sciences* **121**, e2321665121 (2024).
34. Xu, Y. *et al.* Correlated insulating states at fractional fillings of moiré superlattices. *Nature* **587**, 214–218 (2020).

35. Shree, S., Paradisanos, I., Marie, X., Robert, C. & Urbaszek, B. Guide to optical spectroscopy of layered semiconductors. *Nat Rev Phys* **3**, 39–54 (2021).
36. Jin, C. *et al.* Ultrafast dynamics in van der Waals heterostructures. *Nature Nanotech* **13**, 994–1003 (2018).
37. Raja, A. *et al.* Coulomb engineering of the bandgap and excitons in two-dimensional materials. *Nat Commun* **8**, 15251 (2017).
38. Landau, L. D. The Theory of a Fermi Liquid. *Zh. Eksp. Teor. Fiz.* **30**, 1058 (1956).
39. Regan, E. C. *et al.* Mott and generalized Wigner crystal states in WSe₂/WS₂ moiré superlattices. *Nature* **579**, 359–363 (2020).
40. Tang, Y. *et al.* Simulation of Hubbard model physics in WSe₂/WS₂ moiré superlattices. *Nature* **579**, 353–358 (2020).
41. Li, T. *et al.* Continuous Mott transition in semiconductor moiré superlattices. *Nature* **597**, 350–354 (2021).
42. Reddy, A. P., Alsallom, F., Zhang, Y., Devakul, T. & Fu, L. Fractional quantum anomalous Hall states in twisted bilayer MoTe₂ and WSe₂. *Phys. Rev. B* **108**, 085117 (2023).
43. Xie, M., Hafezi, M. & Sarma, S. D. Long-lived Topological Flatband Excitons in Semiconductor Moiré Heterostructures: a Bosonic Kane-Mele Model Platform. Preprint at <https://doi.org/10.48550/arXiv.2403.00052> (2024).
44. Wang, L. *et al.* One-Dimensional Electrical Contact to a Two-Dimensional Material. *Science* **342**, 614–617 (2013).

45. Popert, A. *et al.* Optical Sensing of Fractional Quantum Hall Effect in Graphene. *Nano Lett.* **22**, 7363–7369 (2022).
46. Gu, J. *et al.* Remote imprinting of moiré lattices. *Nat. Mater.* **23**, 219–223 (2024).
47. Zhang, Z. *et al.* Correlated interlayer exciton insulator in heterostructures of monolayer WSe₂ and moiré WS₂/WSe₂. *Nat. Phys.* **18**, 1214–1220 (2022).

Figures

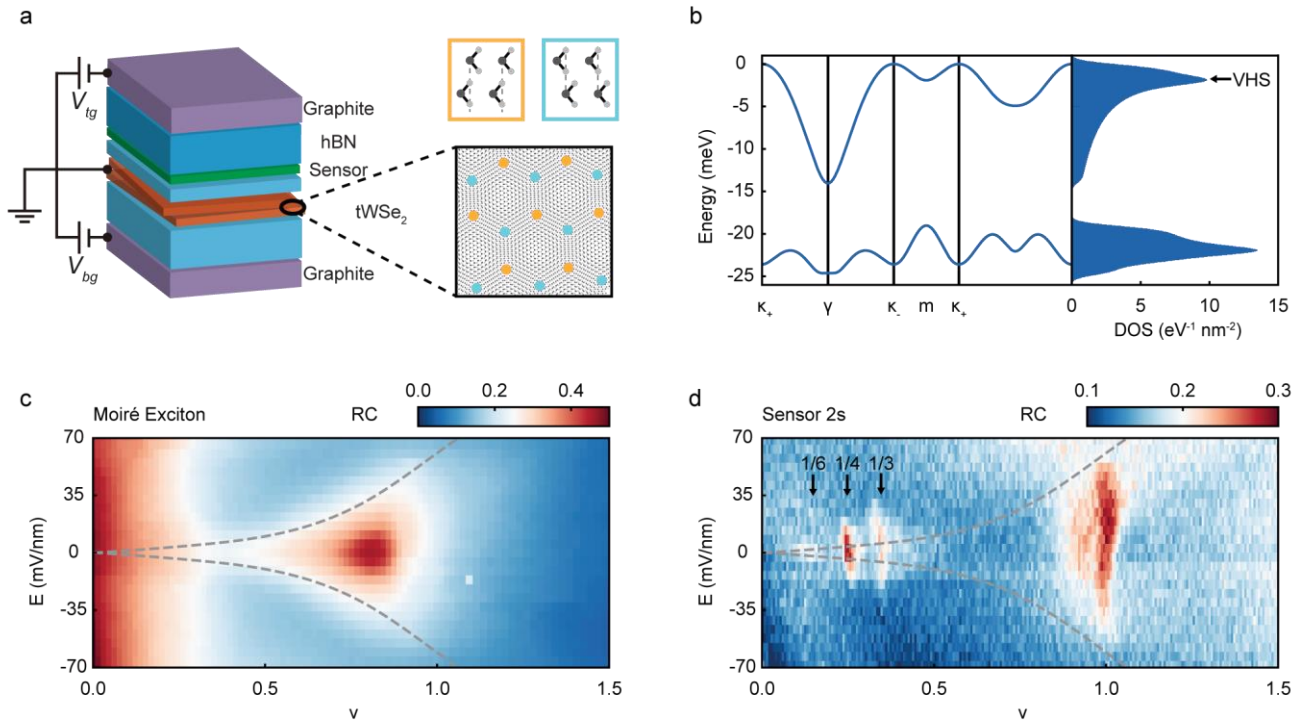


Figure 1 | Experimental setup and phase diagram. **a**, Schematic of a dual-gated 2.7-degree $tWSe_2$ device incorporating a WS_2 sensor layer. Right: the moiré lattice with the MX (orange) and XM (blue) sites labeled ($M = W$ and $X = Se$). The interlayer potential is tunable by a perpendicular electric field. **b**, Continuum model band structure of 2.7-degree $tWSe_2$ (left) and density of states (right) at zero interlayer potential. The VHS is labeled. **c,d**, Spectrally integrated optical reflection contrast for the moiré exciton of the sample (**c**) and for the 2s Rydberg exciton of the sensing layer (**d**) as a function of ν and E at $T = 1.6$ K. The dashed lines separate the low electric field, layer-hybridized region (with high reflection contrast in **c**) from the high electric field, layer-polarized region (with low reflection contrast in **c**).

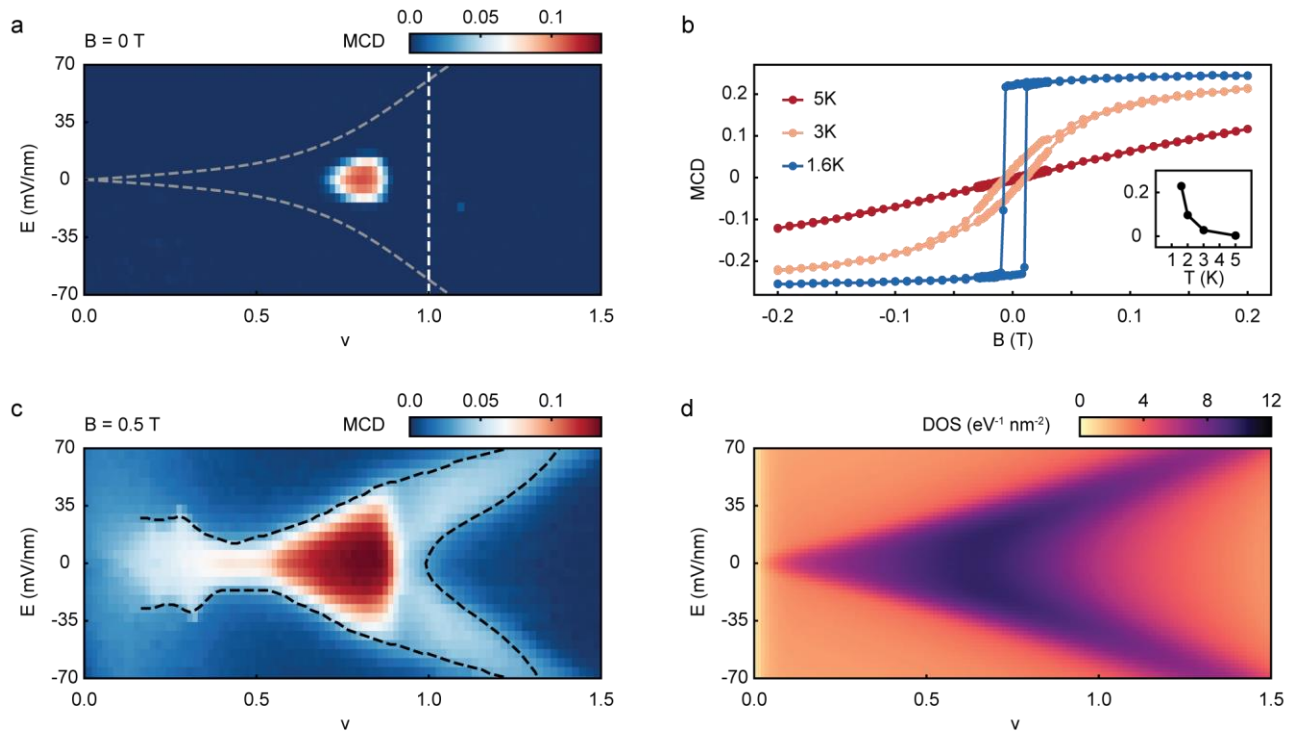


Figure 2 | Electric field tuned van Hove singularity and Stoner ferromagnetism. a, Spectrally averaged spontaneous MCD as a function of ν and E at $T = 1.6$ K. The vertical dashed line marks $\nu = 1$. The dashed lines separating the layer-hybridized and π -polarized regions are also shown. **b,** Magnetic field dependent MCD at the hot spot in **a** and at different temperatures demonstrating magnetic hysteresis and spontaneous time-reversal symmetry breaking. Inset: temperature dependence of the spontaneous MCD. **c,** Spectrally averaged MCD at $B = 0.5$ T as a function of ν and E at $T = 1.6$ K. The dashed lines outline the region with enhanced magnetic susceptibility (except at the ferromagnetic region). **d,** Calculated DOS as a function of ν and E showing the evolution of the VHS with E .

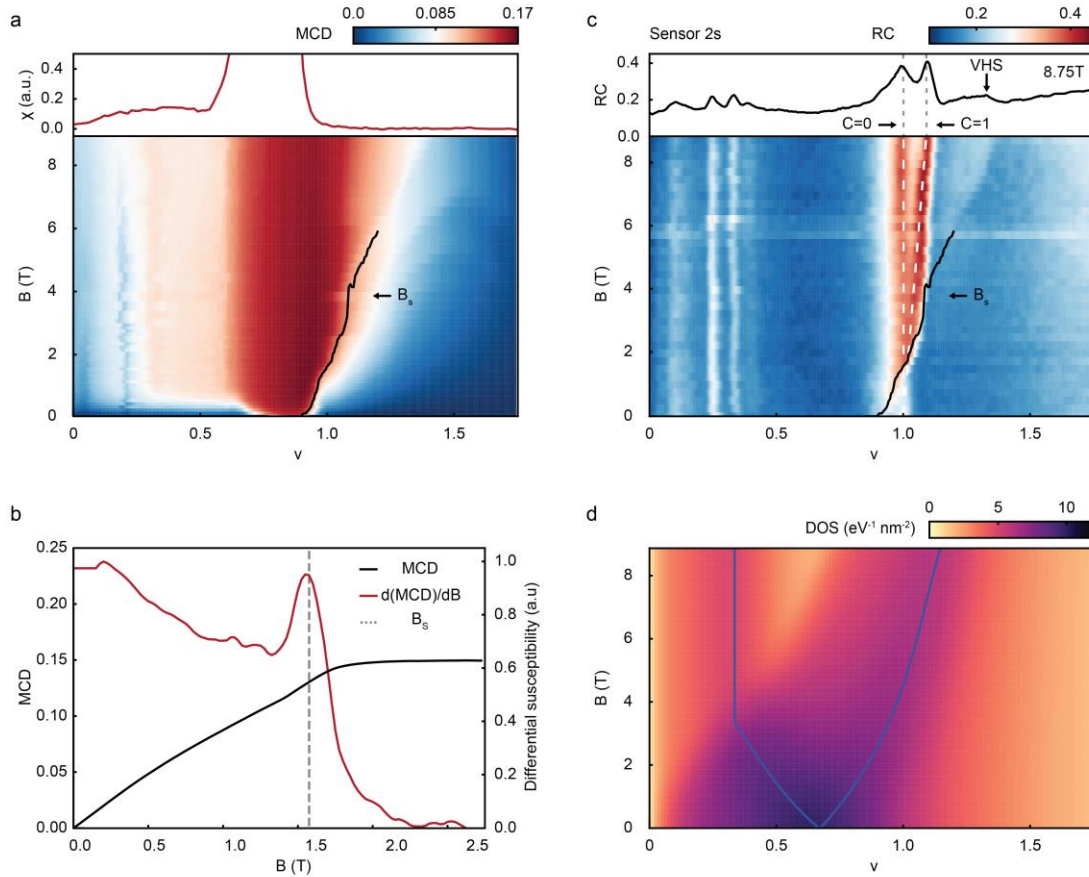


Figure 3 | Van Hove singularity, valley polarization and Chern insulator. **a**, Spectrally averaged MCD as a function of ν and B at $T = 1.6$ K ($E = 0$). The black curve shows the density dependence of the saturation field B_s . Top: Density dependence of the magnetic susceptibility χ extracted from the small field MCD. **b**, A line cut at $\nu = 1$ in **a** showing the magnetic field dependent MCD (black) and its field derivative (or differential magnetic susceptibility, red). The differential susceptibility peak corresponds to a MCD bump near B_s , which is marked by the vertical dashed line. **c**, Spectrally integrated optical reflection contrast for the 2s Rydberg exciton of the sensing layer as a function of ν and B at $T = 1.6$ K. The density dependence of B_s is also shown. White dashed lines denote the expected dispersions for states with Chern numbers 0 and 1. Top: Line cut at $B = 8.75$ T. The arrow marks the location of the VHS. **d**, Calculated DOS as a function of ν and B showing the Zeeman splitting of the VHS traced by the blue curves.

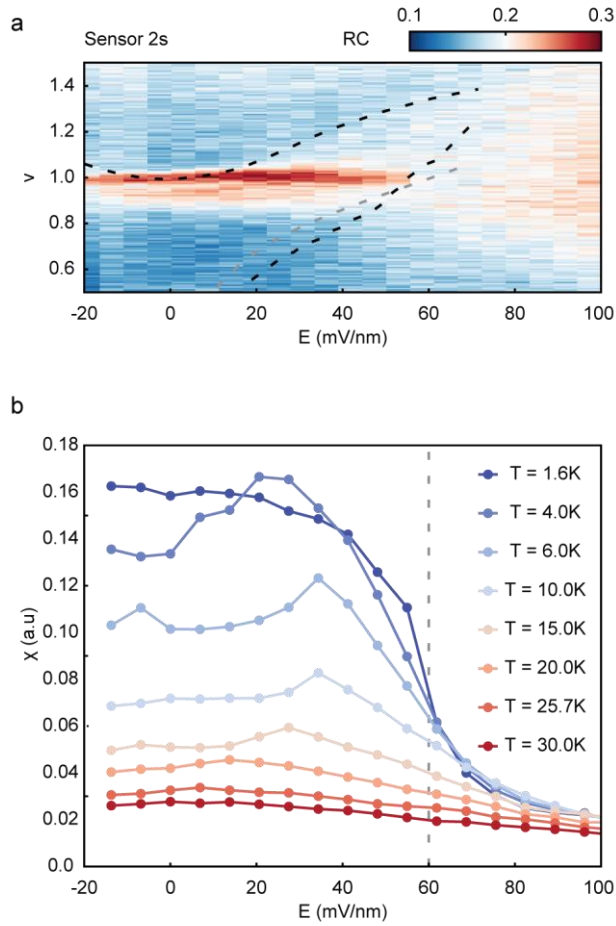
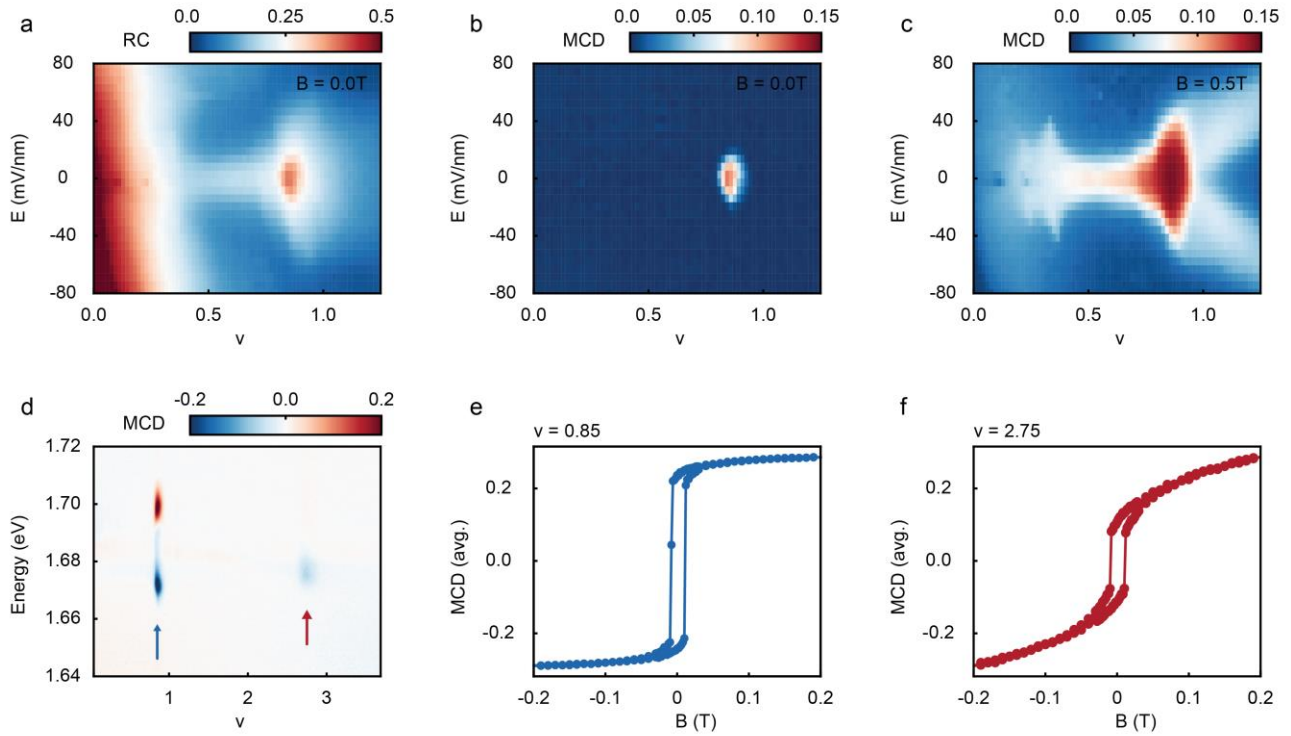
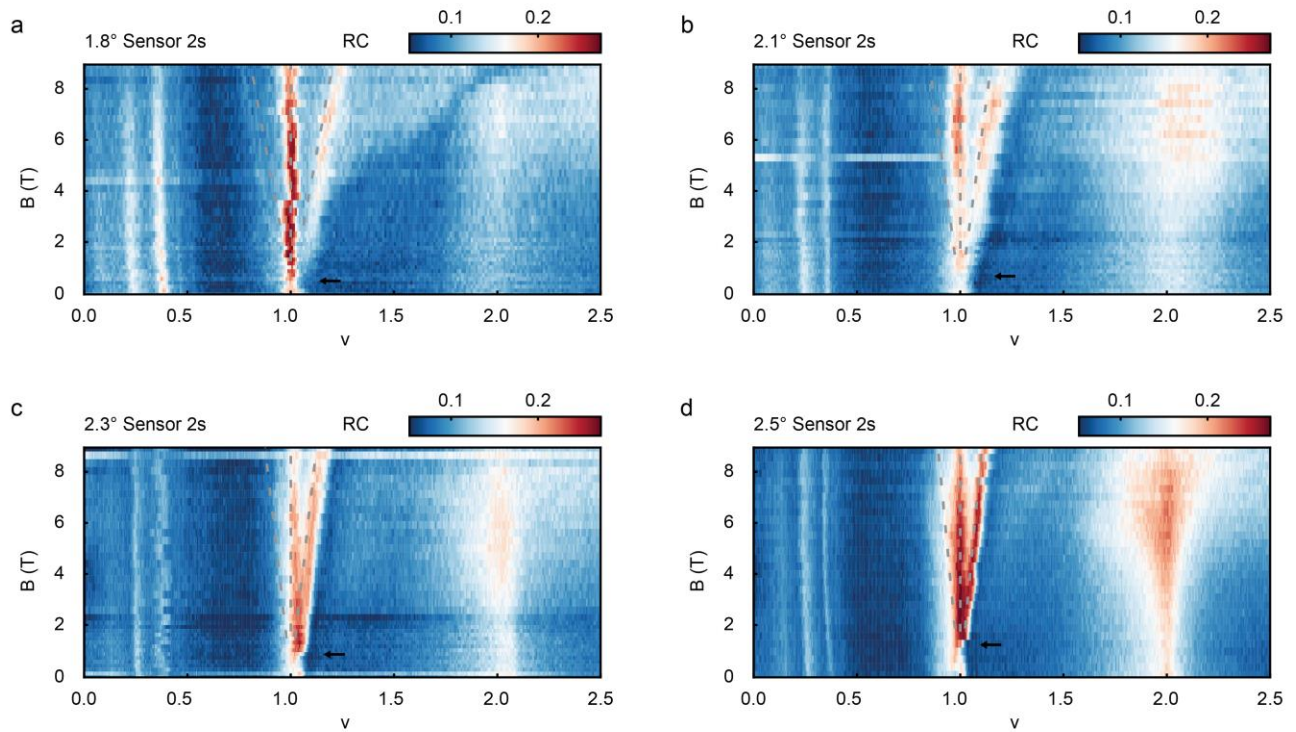


Figure 4 | Van Hove singularity, layer polarization and metal-insulator transition. a, Spectrally integrated optical reflection contrast for the 2s Rydberg exciton of the sensing layer as a function of ν and E at $T = 1.6$ K. An electric field tuned MIT is observed at $\nu = 1$. Black dashed lines mark the region of enhanced magnetic susceptibility in **Fig. 2c**; grey dashed line shows the layer polarization boundary in **Fig. 1c**. **b,** Small field MCD, proportional to the magnetic susceptibility χ , as a function of E at different temperatures. A change from Curie-Weiss to Pauli susceptibility is observed at the MIT critical point (dashed line).

Extended Data Figures

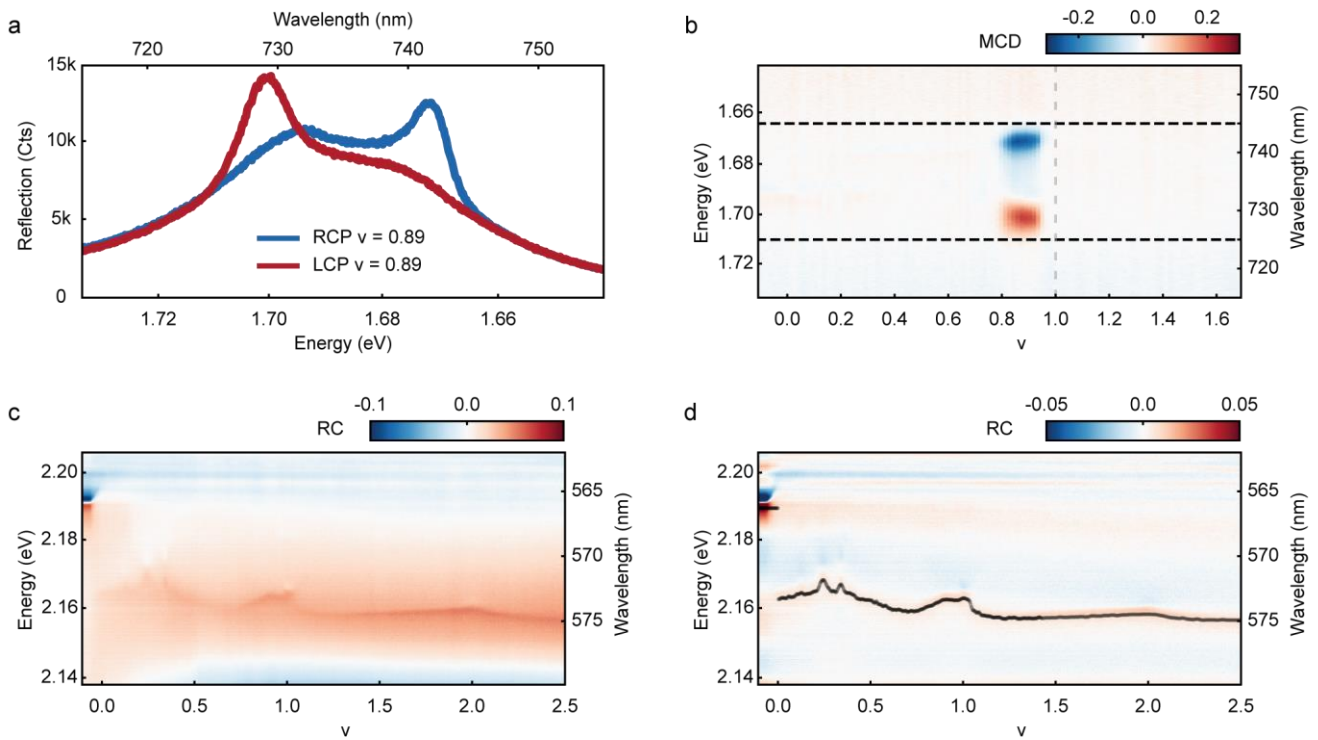


Extended Data Figure 1 | Ferromagnetism at smaller twist angle $\theta = 2.5^\circ$ at $T = 1.6$ K. **a**, Reflection contrast of the moiré exciton as a function of ν and E **b**, Spontaneous MCD ($B = 0$ T) and **c**, small field MCD ($B = 0.5$ T), both as a function of ν and E . **d**, Spontaneous magnetization ($B = 0$ T, $T = 1.6$ K) evidenced by the filling factor dependent MCD spectra at zero electric field. The arrows mark the emergence of ferromagnetism at $\nu = 0.85$ and 2.75 . **e,f**, Magnetic hysteresis loop measured at $\nu = 0.85$ (**e** blue arrow in **f**) and at $\nu = 2.75$ (**e** red arrow in **c**).

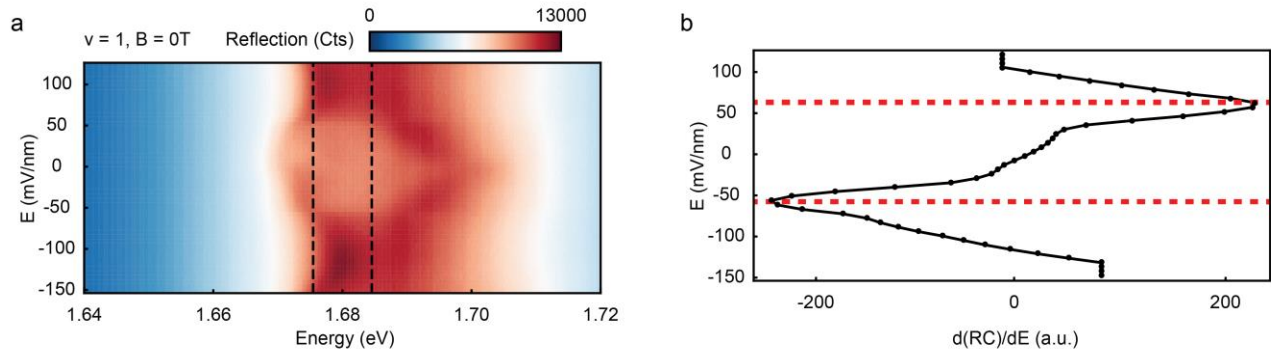


Extended Data Figure 2 | Twist angle dependence of the correlated insulating states.

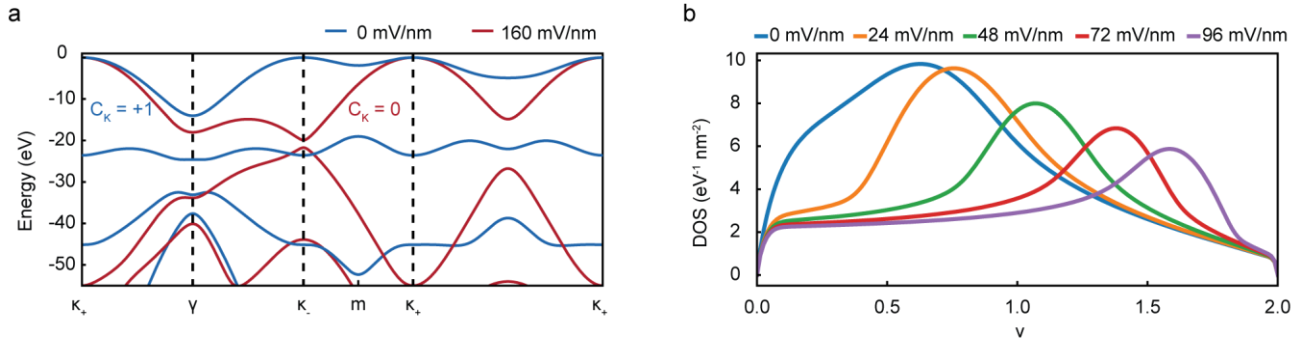
a-d, Spectrally integrated optical reflection contrast for the 2s Rydberg exciton of the sensing layer as a function of ν and B at $T = 1.6$ K for twist angles 1.8° - 2.5° . Grey dashed lines denote the expected dispersions for states with Chern numbers 0 and ± 1 near $\nu = 1$. In general, decreasing the twist angle lowers the saturation magnetic field at $\nu = 1$ (arrows) and correspondingly the magnetic field for the emergence of the $c = +1$ Chern insulator. At twist angle 1.8° , a weak $c = -1$ Chern insulating state also emerges and coexists with the $c = +1$ Chern insulator. The states at fractional fillings and at $\nu = 2$ do not disperse with magnetic fields and are not Chern insulators.



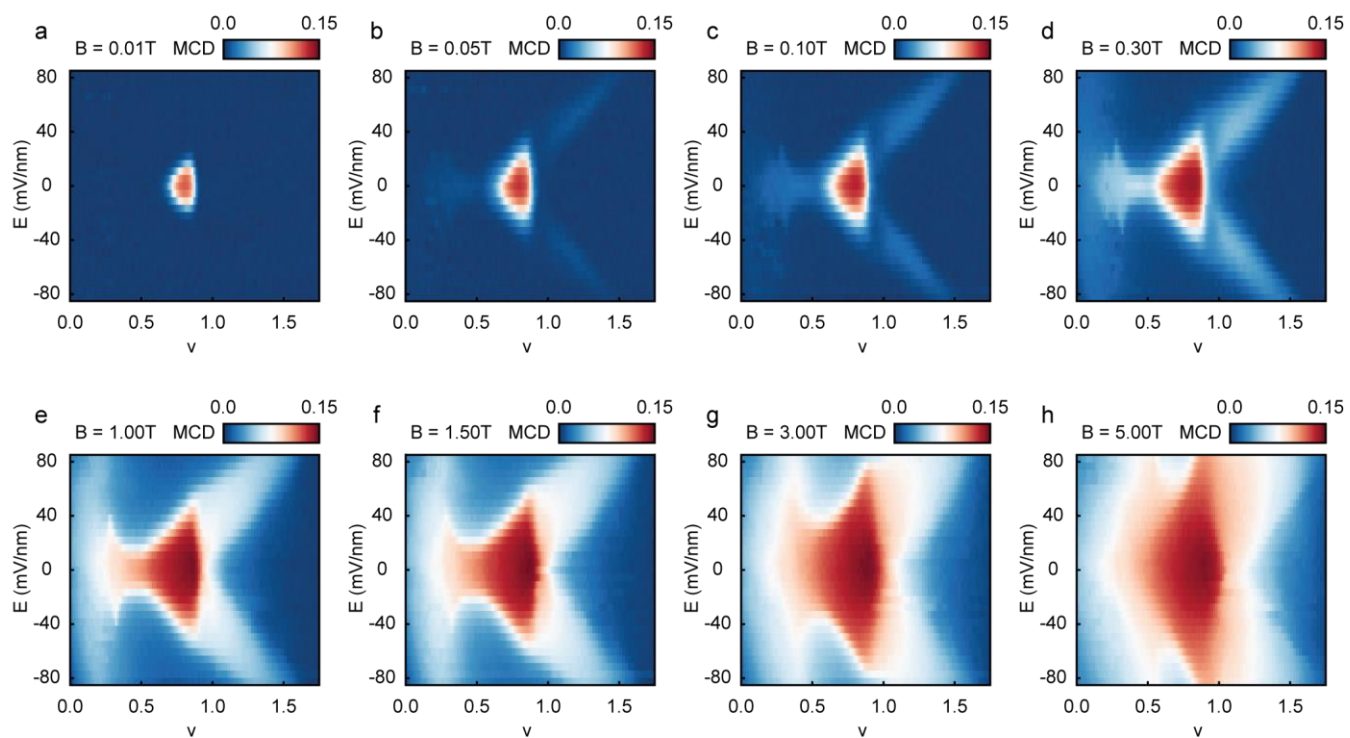
Extended Data Figure 3 | Moiré exciton, MCD and 2s reflection spectra. **a**, Left- (LCP) and right-handed (RCP) optical reflection spectrum near the moiré exciton resonance of the 2.7° -degree $tWSe_2$ sample ($\nu = 0.89$, $E = 0$, $B = 0$ and $T = 1.6$ K). **b**, Spontaneous magnetization evidenced by the filling factor dependent MCD spectra at zero magnetic and electric fields. The vertical dashed line marks $\nu = 1$; the horizontal dashed lines bound the spectral window, over which we average the absolute value of the MCD signal to obtain the spectrally averaged MCD. **c**, Filling factor dependence of the reflection contrast spectrum near the 2s exciton resonance of the sensing layer. **d**, The corresponding spectrum after removal of a smooth background to emphasize the 2s resonance. The black curve traces the 2s resonance. A 2 nm spectral window is opened around the 2s resonance in order to obtain the spectrally integrated reflection contrast.



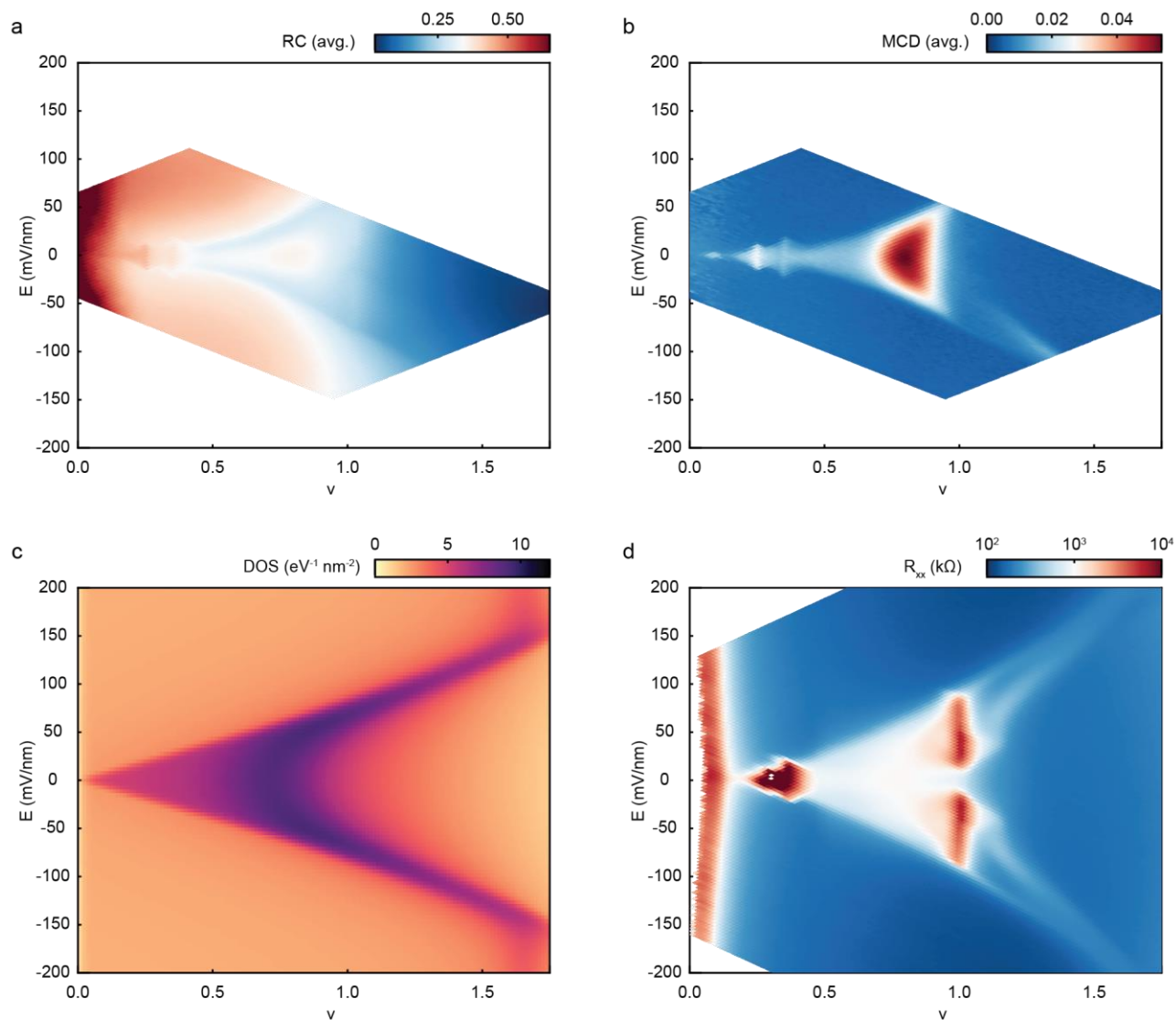
Extended Data Figure 4 | Determination of the critical electric field for layer polarization. **a**, Electric field dependent optical reflection spectrum near the $tWSe_2$ moiré exciton resonance at $\nu = 1$, $B = 0$ and $T = 1.6$ K. We integrate the signal over the spectral window bound by the dashed lines to obtain the integrated reflection contrast. **b**, The electric field derivative of the integrated reflection contrast plotted as a function of the electric field. The red dashed lines mark the maximum and minimum, which define the phase boundary between the layer-hybridized and layer-polarized states in the phase diagram as shown in **Fig. 1c**.



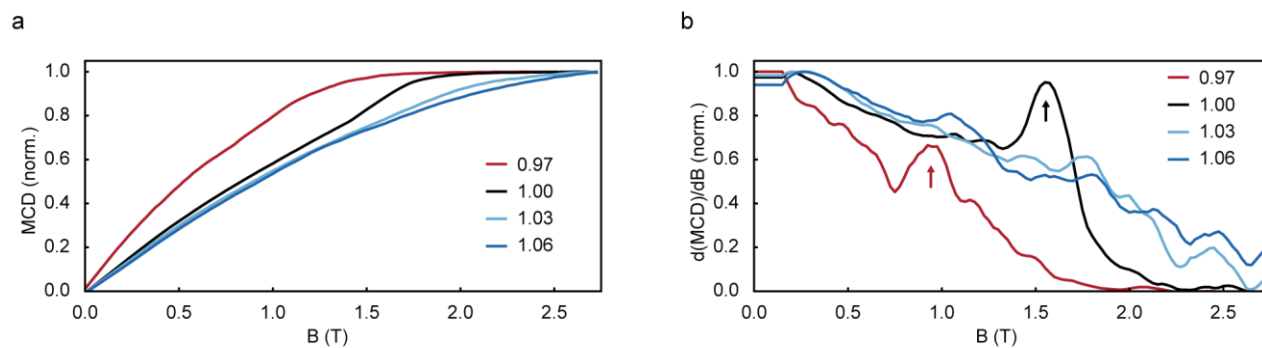
Extended Data Figure 5 | Continuum model bands at different electric fields. a, Continuum model band structure of 2.7-degree tWSe₂ at two electric fields. The bands become more dispersive under a finite electric field. **b,** Filling factor dependence of the electronic DOS at different electric fields. The VHS weakens and disperses to higher filling factors with increasing E .



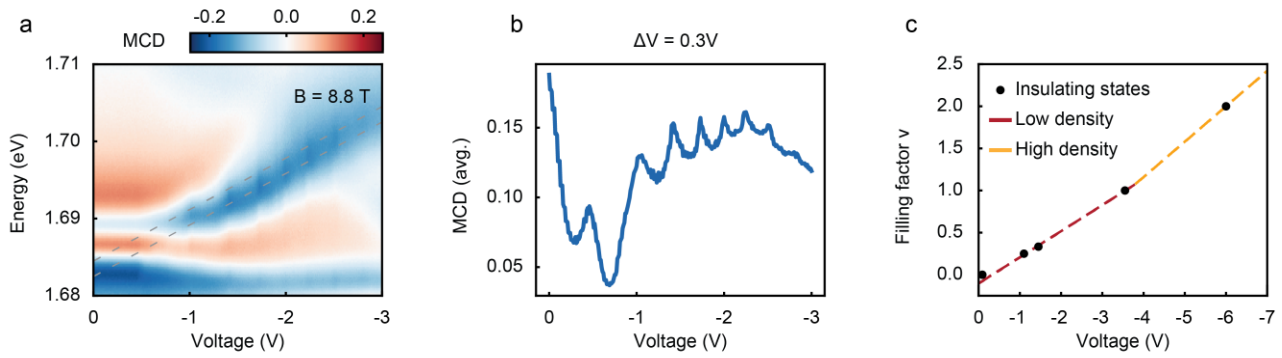
Extended Data Figure 6 | Spectrally averaged MCD as a function of ν and E at $T = 1.6$ K and varying magnetic fields.



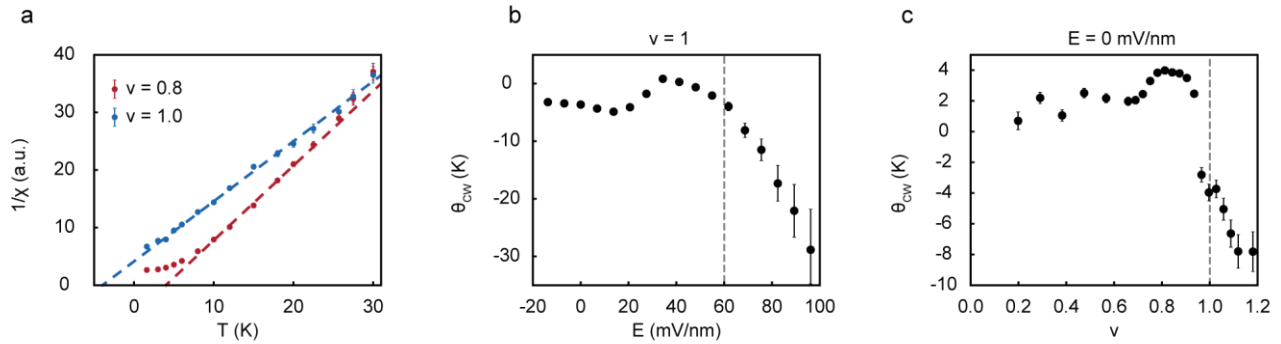
Extended Data Figure 7 | Comparison of electrical and optical measurements on samples with 3.5° twist angle. **a,b**, Spectrally averaged optical reflection contrast for the moiré exciton of the sample **(a)** and the corresponding spectrally averaged MCD **(b)** as a function of ν and E at $T = 1.6$ K. **c**, Calculated DOS as a function of ν and E showing the evolution of the VHS with E . **d**, The longitudinal resistance as a function of ν and E at $T = 1.6$ K. All measurements were taken at $B = 0.1$ T.



Extended Data Figure 8 | Magnetic field dependent MCD and differential susceptibility at varying fillings. **a**, Magnetic field dependent MCD (normalized to the saturation value) at varying filling factors ($E = 0$ and $T = 1.6$ K). **b**, The corresponding field derivative (or differential magnetic susceptibility) versus B . The differential susceptibility peaks correspond to the MCD bumps near B_s at $\nu = 0.97$ and 1 (marked by arrows).



Extended Data Figure 9 | Carrier density calibration for twist angle $\theta = 2.7^\circ$. **a**, MCD spectrum near the moiré exciton resonance of the tWSe₂ sample as a function of the doping voltage (from symmetric gating) at $B = 8.8$ T and $T = 1.6$ K. The periodic MCD modulations inside the region bound by the grey dashed lines show the formation of LLs. **b**, Spectrally averaged MCD over the spectral window bound by the dashed lines in **a** plotted against the doping voltage. The peaks with periodicity of $\Delta V = 0.3$ V yield a measurement of the hole density **c**, The filling factor for the insulating states (obtained from 2s sensing) versus the doping voltage. A two-piece linear interpolation is used to convert the voltage to filling factor and to obtain the moiré density and twist angle (see Methods).



Extended Data Figure 10 | Curie-Weiss analysis of the magnetic susceptibility. **a**, Inverse magnetic susceptibility as approximated by the small-field MCD slope versus temperature at different filling factors ($E = 0$). The dashed lines show the Curie-Weiss fits to the data above 10 K. **b**, The extracted Curie-Weiss (CW) temperature versus E at $\nu = 1$. The dashed line marks the MIT critical electric field. The small CW temperature in the insulator regime corresponds a strong temperature dependence for the magnetic susceptibility, a typical behavior for a system with local magnetic moments. The negative CW temperature shows an antiferromagnetic interaction between the local moments in this regime. The CW temperature turns much more negative in the metallic regime; it corresponds to the emergence of Fermi pressure from a Fermi liquid. The behavior corresponds to a weak temperature dependence for the magnetic susceptibility in this regime. **c**, Filling factor dependence of the CW temperature at $E = 0$. A positive CW temperature with a peak is seen near $\nu = 0.85$, consistent with the emergence of ferromagnetism in the sample. The CW temperature turns negative at $\nu = 1$ as the interaction between the local moments turns antiferromagnetic. The negative CW temperature for $\nu > 1$ is due to the Fermi pressure of a Fermi liquid.